JOURNAL OF AIRCRAFT
Vol. 31, No. 3, May–June 1994

Numerical Investigations on Two-Dimensional Canard-Wing Aerodynamic Interference

San-Yih Lin,* Yan-Shin Chin,† and Yuh-Ying Wang†
Institute of Aeronautics and Astronautics, Tainan, Taiwan, Republic of China

A finite element method for solving of the Euler and Navier-Stokes equations is used to study the unsteady aerodynamics of a two-dimensional canard-wing aerodynamic interference. The method used a discontinuous finite element method for spatial discretization and an explicit Runge-Kutta time integration for temporal discretization. The problems of a flow over an airfoil with/without viscosity, a flow over a pitching airfoil, and an airfoil-vortex interaction are tested to show the accuracy of the proposed numerical method. Finally, the results of two-dimensional canard-wing aerodynamic interference in steady and unsteady transonic flows are shown to demonstrate the robustness of the numerical algorithm, and qualitative and quantitative aerodynamic influence of one airfoil on the other.

I. Introduction

A NUMBER of highly maneuverable fighter configurations has been proposed with closely coupled canard systems which can lead to several advantages, such as higher trimmed-lift capability, improving pitching moment characteristics, and reducing trim drag at transonic speeds. To clearly understand the closely coupled canard-wing interference flowfields, a two-dimensional inviscid Euler model is studied in the present investigation.

Many of the numerical schemes for solving such problems are based on the transonic small-disturbance (TSD) potential equations. Steady transonic flowfields and interference effects of two- and three-dimensional canard-wing systems have been studied by Shankar et al.[1,2] using TSD and modified TSD. Agrell and Elmeland[3] compared the TSD method with a linearized panel method for a low aspect ratio canard in various Mach numbers. Unsteady transonic flow calculations for two- and three-dimensional canard-wing interaction problems have been performed by Batina et al.[4,5] using unsteady transonic small-disturbance codes called XTRAN2L and XTRAN3S. However, schemes based on the potential equations are somewhat limited in scope, because the assumptions of ignoring entropy changes and vorticity production across the shock are not strictly correct. The objectives of the study are 1) to develop an unsteady transonic Euler solver with dynamic grid system for aerodynamically interfering airfoils, 2) to qualitatively and quantitatively discuss the effects of Mach and Reynolds numbers on the flow qualities, and 3) to investigate the effects of two-dimensional canard-wing aerodynamic interference in steady and unsteady transonic flows.

A finite element method for solving the Euler and Navier-Stokes equations is used to study the above subjects. The method used a discontinuous finite element method for spatial discretization and an explicit Runge-Kutta time integration for temporal discretization. A dynamic grid method is used in the proposed method to simulate flows over airfoils in pitching motion. The outlines of the numerical procedure are presented in Sec. II. In Sec. III, the problems of a flow over an airfoil with/without viscosity, a flow over a pitching airfoil, and an airfoil-vortex interaction are tested to show the accuracy of the proposed numerical method. On the flow over an airfoil, we discuss the effects of Mach and Reynolds numbers on the flowfields. Finally, in Sec. IV, we present the results of two-dimensional canard-wing aerodynamic interference in steady and unsteady transonic flows to demonstrate the robustness of the numerical algorithm, and qualitative and quantitative aerodynamic influence of one airfoil on the other.

Received Sept. 11, 1992; presented as Paper 93-0639 at the AIAA 31st Aerospace Sciences Meeting, Reno, NV, Jan. 11–14, 1993; revision received April 21, 1993; accepted for publication July 24, 1993.

*Associate Professor, National Cheng Kung University, supported in part by the National Science Council. Member AIAA.
†Graduate Student, National Cheng Kung University, supported in part by the National Science Council.

II. Numerical Method

A. Governing Equations

The two-dimensional, compressible, and inviscid/viscous flows can be described in conservation form by the Euler/Navier-Stokes equations:

$$w_t + \nabla \cdot (f, g) = 0 \tag{1}$$

where

$$w = \begin{bmatrix} \rho \\ \rho u \\ \rho v \\ \rho e \end{bmatrix}, \quad f = \begin{bmatrix} f_1 \\ f_2 \\ f_3 \\ f_4 \end{bmatrix} = \begin{bmatrix} \rho u \\ \rho u^2 + p - (1/Re)\tau_{xx} \\ \rho uv - (1/Re)\tau_{xy} \\ u(\rho e + p) - (1/Re)r_4 \end{bmatrix}$$

$$g = \begin{bmatrix} g_1 \\ g_2 \\ g_3 \\ g_4 \end{bmatrix} = \begin{bmatrix} \rho v \\ \rho uv - (1/Re)\tau_{xy} \\ \rho v^2 + p - (1/Re)\tau_{yy} \\ v(\rho e + p) - (1/Re)s_4 \end{bmatrix}$$

with

$$\tau_{xx} = \mu(4u_x - 2v_y)/3$$

$$\tau_{xy} = \mu(u_y + v_x)$$

$$\tau_{yy} = \mu(-2u_x + 4v_y)/3$$

$$r_4 = u\tau_{xx} + v\tau_{xy} + \frac{\mu}{Pr(\gamma - 1)}(a^2)_x$$

$$s_4 = u\tau_{xy} + v\tau_{yy} + \frac{\mu}{Pr(\gamma - 1)}(a^2)_y$$

here, p, ρ, u, v, and e are the pressure, density, x- and y-direction velocity components, and the total energy per unit mass, respectively. μ is the dynamic viscosity determined by Sutherland's law. The Reynolds number and Prandtl number are denoted as Re and Pr, respectively. a is the speed of sound.

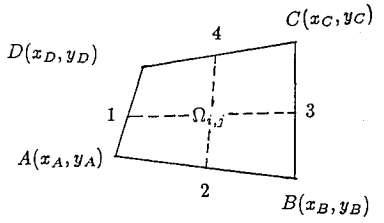

Fig. 1 Representation of quadrilateral Ω_{ij}.

The pressure p is given by the equation of state for a perfect gas

$$p = (\gamma - 1)[\rho e - \tfrac{1}{2}\rho(u^2 + v^2)]$$

where γ ($=1.4$ for air) is the ratio of specific heats.

B. Space Discretization—The Discontinuous Finite Element Method

The method used is based on a two-step modified Runge-Kutta time integration coupling with a discontinuous finite element method. Only an outline of the numerical method is presented in Secs. II.B., II.C., and II.D. A detailed development can be found in Ref. 6.

Ω is the computed domain, $\{\Omega_{ij}\}$ is a quadrilateral partition of Ω, and $\partial\Omega_{ij}$ is the boundary of Ω_{ij}. In this article we approximate any function w as

$$w_h(x, y; t) = w^0(t) + \tilde{w}(t)\tilde{\phi}(x, y) + \tilde{\tilde{w}}(t)\tilde{\tilde{\phi}}(x, y) \quad \text{for} \quad (x, y) \in \Omega_{ij} \tag{2}$$

where Ω_{ij} is an arbitrary quadrilateral. In Fig. 1, A, B, C, and D are the vertices of Ω_{ij}, and 1, 2, 3, and 4 are the midpoints of the edges of Ω_{ij}, respectively. $\tilde{\phi}$ and $\tilde{\tilde{\phi}}$ are defined as the following. First, we transform the quadrilateral Ω_{ij} into a square Ω'_{ij} in $\xi\eta$ plane by a bilinear transform function $T(\xi, \eta)$, where $\Omega'_{ij} = [(\xi, \eta), -1 \le \xi \le 1, -1 \le \eta \le 1]$. Then, $\tilde{\phi}$ and $\tilde{\tilde{\phi}}$ are defined as

$$\begin{aligned} \tilde{\phi}(x, y) &= \tilde{\phi}[x(\xi, \eta), y(\xi, \eta)] = \tilde{\phi}'(\xi, \eta) = \xi \\ \tilde{\tilde{\phi}}(x, y) &= \tilde{\tilde{\phi}}[x(\xi, \eta), y(\xi, \eta)] = \tilde{\tilde{\phi}}'(\xi, \eta) = \eta \end{aligned} \tag{3}$$

Note that $\tilde{\phi}$ and $\tilde{\tilde{\phi}}$ are close to linear functions such that

$$\tilde{\phi}(x, y) = \begin{cases} 1, & (x, y) \in \overline{BC} \\ 0, & (x, y) \in \overline{24}, \\ -1, & (x, y) \in \overline{AD} \end{cases} \quad (x, y) \in \Omega_{ij}$$

$$\tilde{\tilde{\phi}}(x, y) = \begin{cases} 1, & (x, y) \in \overline{CD} \\ 0, & (x, y) \in \overline{13}, \\ -1, & (x, y) \in \overline{AB} \end{cases} \quad (x, y) \in \Omega_{ij}$$

And, they are allowed to have jumps at the interface between two quadrilaterals to capture the discontinuities of the solutions. Now, multiplying Eq. (1) by φ and integrating over an arbitrarily moving subdomain $\Omega_{ij}(t)$, we have

$$\int\int_{\Omega_{ij}(t)} \frac{\partial w}{\partial t}\varphi \, dx \, dy + \int\int_{\Omega_{ij}(t)} \nabla\cdot(f, g)\varphi \, dx \, dy = 0 \tag{4}$$

Assuming $\varphi = 1$, $\varphi = \tilde{\phi}$, and $\varphi = \tilde{\tilde{\phi}}$, we can obtain the following equations:

$$\frac{d}{dt}(w^0 A_{ij}) = -\int_{\partial\Omega_{ij}(t)} (Fn_x + Gn_y)\, dl \tag{5a}$$

$$\frac{d}{dt}\left(\frac{\tilde{w}A_{ij}}{3}\right) = -\int_{\partial\Omega_{ij}(t)} (Fn_x + Gn_y)\tilde{\phi}\, dl + \int\int_{\Omega_{ij}(t)} (F\tilde{\phi}_x + G\tilde{\phi}_y)\, dx\, dy \tag{5b}$$

$$\frac{d}{dt}\left(\frac{\tilde{\tilde{w}}A_{ij}}{3}\right) = -\int_{\partial\Omega_{ij}(t)} (Fn_x + Gn_y)\tilde{\tilde{\phi}}\, dl + \int\int_{\Omega_{ij}(t)} (F\tilde{\tilde{\phi}}_x + G\tilde{\tilde{\phi}}_y)\, dx\, dy \tag{5c}$$

where A_{ij} is the area of $\Omega_{ij}(t)$, (n_x, n_y) is an outward normal vector of the quadrilateral Ω_{ij}, and

$$F = \begin{bmatrix} f_1 - \rho x_t \\ f_2 - \rho u x_t \\ f_3 - \rho v x_t \\ f_4 - \rho e x_t + p x_t \end{bmatrix}$$

$$G = \begin{bmatrix} g_1 - \rho y_t \\ g_2 - \rho u y_t \\ g_3 - \rho v y_t \\ g_4 - \rho e y_t + p y_t \end{bmatrix}$$

where x_t and y_t are the grid speeds in the x and y directions (for a fixed grid system, $x_t = y_t = 0$). The line integrals in the equations are estimated by the midpoint integral rule with some kinds of upwind techniques, and the surface integrals are estimated by the quadrature numerical integrations. Details of the derivations are given in Ref. 6.

C. Time Integration—The Two-Step Runge-Kutta Method

Rewrite the ordinary differential Eq. (5) as

$$\frac{dw}{dt} = H(w)$$

$$w = \begin{pmatrix} w^0 \\ \tilde{w} \\ \tilde{\tilde{w}} \end{pmatrix}$$

The following two-step Runge-Kutta time integration[6] is used. For a given w^n at time t_n, we compute w^{n+1} at time t_{n+1} as

$$\begin{aligned} w^{(0)} &= w^n \\ w^{(1)} &= \frac{A^n}{A^{n+1}} w^{(0)} - \frac{1}{2}\frac{\Delta t}{A^{n+1}} H[w^{(0)}] \\ w^{(2)} &= \frac{A^n}{A^{n+1}} w^{(0)} - \frac{\Delta t}{A^{n+1}} H[w^{(1)}] \\ w^{n+1} &= w^{(2)} \end{aligned} \tag{6}$$

where A^n and A^{n+1} are the area of Ω_{ij} at time t_n and t_{n+1}, respectively. This time integration is second-order accurate and includes the necessary terms to account for changes in cell areas due to moving grids. We note that a local projection limiting the slopes, $\tilde{w}$ and $\tilde{\tilde{w}}$, is necessarily introduced in the numerical procedure to avoid the numerical wiggles at some critical regions, such as shock and higher gradient regions.[6]

D. Boundary Conditions

We use a standard characteristic boundary condition[6] to compute the far-field boundary conditions. The solid surface boundary condition for inviscid flow is the tangency condition. For viscous flow, the usual no-slip condition is applied, i.e., $u = 0$, $v = 0$ ($u - x_t = 0$, $v - y_t = 0$ for a moving grid system). The density and pressure on the wall surface (see Fig. 2 for grid structure) for inviscid and viscous flows are determined as

$$\rho^b = \rho^1 - \text{minmod}[0.5(\rho^2 - \rho^1), \tilde{\rho}^1]$$
$$p^b = p^1 - 0.5(p^2 - p^1) \tag{7}$$

E. Dynamic Grid Algorithm

A dynamic grid algorithm is included to compute the flows over airfoils in pitching motion. The idea is that we fix the grid points on the outer boundary, correct the grid points on the inner surface boundary according to the moving body, and determine the rest of points by modeling each edge of each cell by a spring. Details of the dynamic grid algorithm are given in Refs. 6–9. By this algorithm, for given $(x_{ij}, y_{ij})^n$ at time t_n and the corresponding surface boundary motion, one can define $(x_{ij}, y_{ij})^{n+1}$ at time t_{n+1}. And the grid speed $(x_t, y_t)^n$ is determined by

$$x_t^n(i,j) = \frac{x_{i,j}^{n+1} - x_{i,j}^{n-1}}{\Delta T_1 + \Delta T_2}$$
$$y_t^n(i,j) = \frac{y_{i,j}^{n+1} - y_{i,j}^{n-1}}{\Delta T_1 + \Delta T_2} \tag{8}$$

here, ΔT_1 is the time step between t_{n-1} and t_n, and ΔT_2 between t_n and t_{n+1}.

In the time marching process, we need to calculate the area of each quadrilateral at every time step. To avoid errors induced by the dynamic grid system, it is necessary to add a geometric conservation law to determine the relationship among the grid points, grid speeds, and the cell areas. Then one can compute the area A^{n+1} as

$$A_{i,j}^{n+1} = A_{i,j}^n + \Delta t \sum_m (x_{t_m}^n \Delta y_m - y_{t_m}^n \Delta x_m) \tag{9}$$

where the summation is taken over all edges of the quadrilateral Ω_{ij}, and Δx, Δy are determined by

$$\Delta x = \frac{\Delta x^{n+1} + \Delta x^n}{2}, \qquad \Delta y = \frac{\Delta y^{n+1} + \Delta y^n}{2}$$

III. Numerical Test Problems

The problems of a flow over a stationary airfoil with/without viscosity, a flow over a pitching airfoil, and an airfoil-vortex interaction are tested to show the accuracy of the proposed numerical method.

A. Flow over a Stationary Airfoil

In this example, we will show the accuracy of the numerical method and discuss the effects of Mach and Reynolds numbers on the flowfields. The single NACA 0012 airfoil computations have to be performed on the 192 × 40 C-type grids for both Euler and Navier-Stokes equations. First we show the result

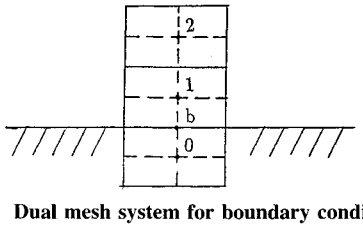

Fig. 2 Dual mesh system for boundary conditions.

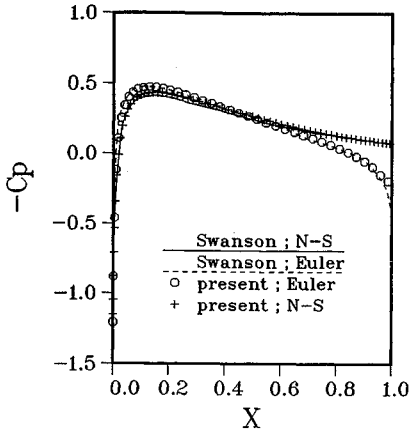

Fig. 3 Pressure distribution for $M_\infty = 0.5$, $\alpha = 0$, and $Re = 0$ or 5.0×10^3.

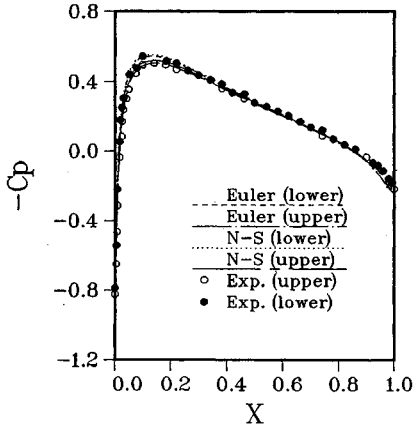

Fig. 4 Pressure distribution for $M_\infty = 0.602$, $\alpha = -0.14$, and $Re = 0$ or 3×10^6.

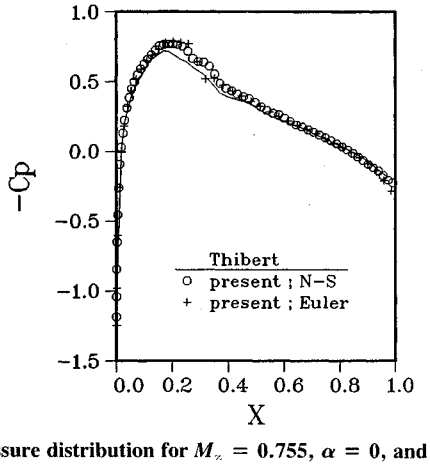

Fig. 5 Pressure distribution for $M_\infty = 0.755$, $\alpha = 0$, and $Re = 0$ or 3×10^6.

on the flow over the airfoil at the freestream Mach number M_∞ of 0.5, 0-deg angle of attack $\alpha = 0$, and $Re = 0$ or 5.0×10^3. Figure 3 shows the surface pressure distribution. In this case, the flow is subsonic and is separated around the tail of the airfoil as $Re = 5.0 \times 10^3$. Therefore, in Fig. 3, one can see a difference between inviscid and viscous flows around the tail. The comparison between ours and Swanson and Turkel's[10] numerical results agrees very well, except at the tail region for the viscous flow computations. Secondly, we show the result on the flow over the airfoil with $M_\infty = 0.602$, $\alpha = -0.14$ deg, and $Re = 0$ or 3×10^6. The flow is subsonic and becomes turbulent as $Re = 3 \times 10^6$. Figure 4 shows the surface pressure distribution which indicates that both inviscid and viscous results are almost the same and agree

well with the experimental data.[11] Finally, we show the result of the flow over the airfoil with $M_\infty = 0.755$, $\alpha = 0$, and $Re = 0$ or 4.01×10^6. The flow is transonic with a weak shock and becomes turbulent as $Re = 4.01 \times 10^6$. Since the weak shock/boundary-layer interaction occurred, the viscous flow has a small separation region at the shock foot. Figure 5 shows the surface pressure distribution. The difference between the inviscid and viscous results is still very small, except at the weak shock/boundary-layer interaction region. Also, the flow is turbulent and one can see the difference between the numerical results and the experimental data.[12] From the above discussions, we conclude that the computational results obtained by the Euler and Navier-Stokes solvers are very close to each other for simulating the transonic flow over a stationary airfoil at higher Reynolds number. Therefore, we use the proposed Euler solver to simulate the rest of the problems.

B. Flow over a Pitching Airfoil

The problem considered is that a NACA 0012 airfoil in a sinusoidal pitching about a fixed point at the quarter chord. The angle of attack varies according to the type

$$\alpha = \alpha_m + \alpha_0 \sin(2kt) \tag{10}$$

where α_m is the mean pitching angle, α_0 is the amplitude of the sinusoidal oscillation, and k is the reduced frequency. Unsteady calculations are started from the converged steady-state solution at $\alpha = \alpha_m$. In this article, we consider $\alpha_m = 0.016$ deg, $\alpha_0 = 2.51$ deg, $k = 0.0814$, and $M_\infty = 0.755$. We compare the surface pressure distribution, lift and moment coefficients with the experimental[13] and numerical data.[8,14] Figure 6 shows the pressure distribution on the airfoil surface which agrees well with the experimental data. They illustrate the movement of shock waves and pressure jumps. The increase of pitching angle induces the increase of flow speed and shock strength on the upper surface. The reverse phenomenon happens on the lower surface of the airfoil. Figure 7 shows the lift and moment coefficients, C_L and C_m. C_m agrees well with the experimental data,[13] except at one point,

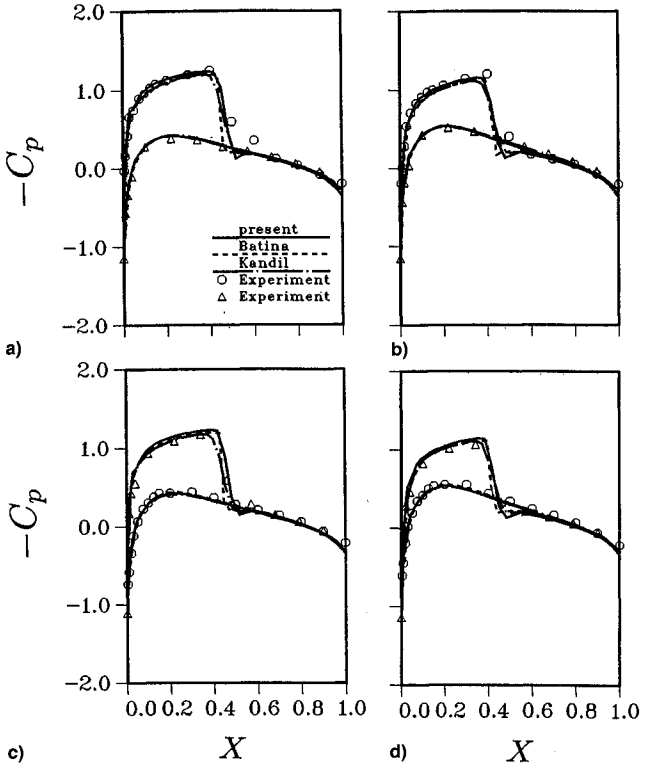

Fig. 6 Instantaneous pressure distribution for a pitching NACA0012 airfoil at phase angle: a) 2.01 deg, b) 0.52 deg, c) −2.0 deg, and d) −0.54 deg.

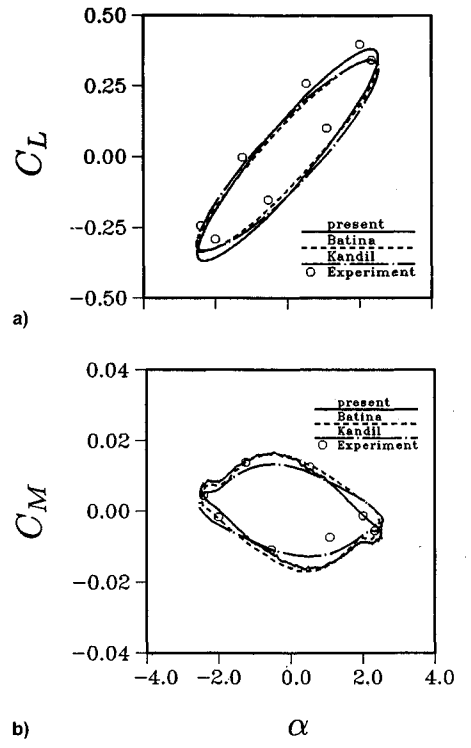

Fig. 7 Instantaneous angle of attack vs a) lift coefficient coefficient and b) moment coefficient.

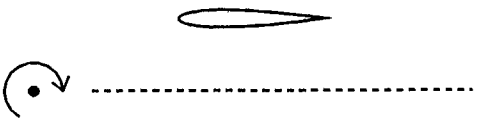

Fig. 8 Schematic of the arrangement of an airfoil-vortex interaction.

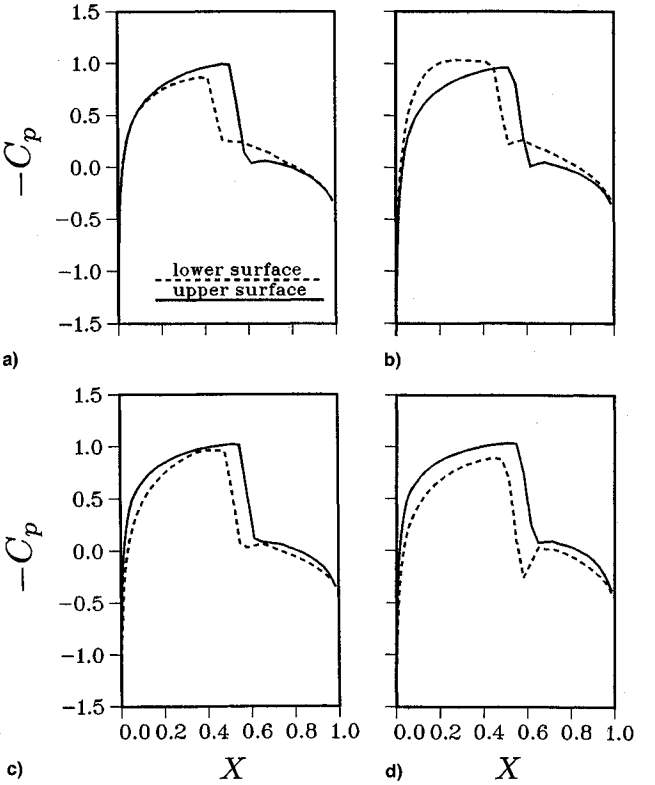

Fig. 9 Pressure distribution on the airfoil at several stages of the vortex passage, t = a) 1.0, b) 2.52, c) 3.42, and d) 4.57.

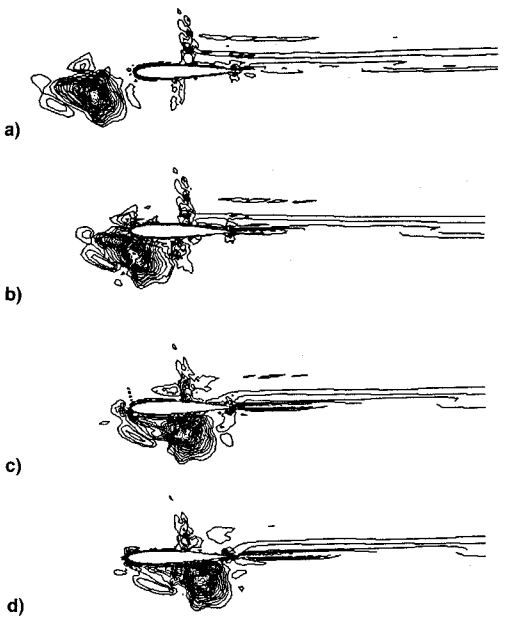

Fig. 10 Vortex contour at several stages of the vortex passage, t = a) 1.0, b) 2.52, c) 3.42, and d) 4.57.

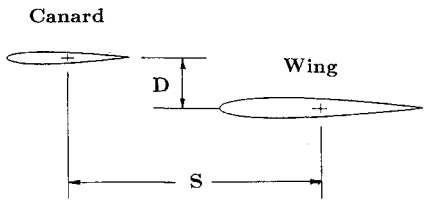

Fig. 11 Schematic of the arrangement of an two-dimensional canard-wing interference.

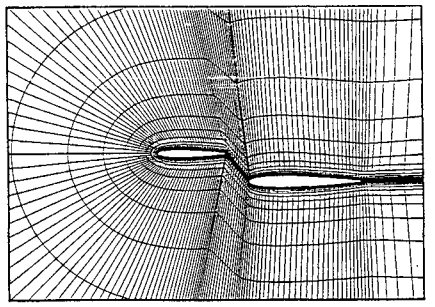

Fig. 12 Grid system for canard-wing with S = 1.0.

α = 1.09 deg. The results indicate that our finite element method combining with the dynamic grid algorithm is suitable for the unsteady transonic problems.

C. Airfoil-Vortex Interaction

The problem describes the airfoil-vortex interaction of a concentrated potential vortex convecting past a stationary airfoil.[15,16] A schematic of the arrangement is shown in Fig. 8. The vortex is initially introduced at $(x_v, y_v) = (-2.0, -0.26)$ with a small disturbance velocity, which is given as

$$u_v = q_v \sin\theta, \qquad v_v = -q_v \cos\theta$$

with

$$q_v = (\Gamma/2\pi r)\{1 - \exp[-(r^2/a^2)]\} \tag{11}$$

where (u_v, v_v) is the disturbance velocity of a concentrated potential vortex superposed in the flow, and (r, θ) is the polar coordinates with the origin at (x_v, y_v). By following McCroskey and Goorjian's paper,[16] we chose Γ = 0.2 and a = 0.05. The "dot line" in Fig. 8 shows the expected path of the vortex. Figure 9 shows the pressure distribution on the airfoil at several stages of the vortex passage. The agreement between our results and McCroskey and Goorjian's results[16] (shown in Fig. 6 in their paper) is satisfactory, except at the time when the vortex is beneath the tail of the airfoil. Figure 10 shows the vorticity contour at several stages of the vortex passage. When the vortex approaches the airfoil, it induces a *downwash* or negative v-velocity perturbation which reduces the lift coefficient. Finally, after the vortex passes the airfoil, it induces an *upwash* v-velocity to the airfoil which increases the lift coefficient. The similar phenomenon will be seen in the following problem of canard-wing interference.

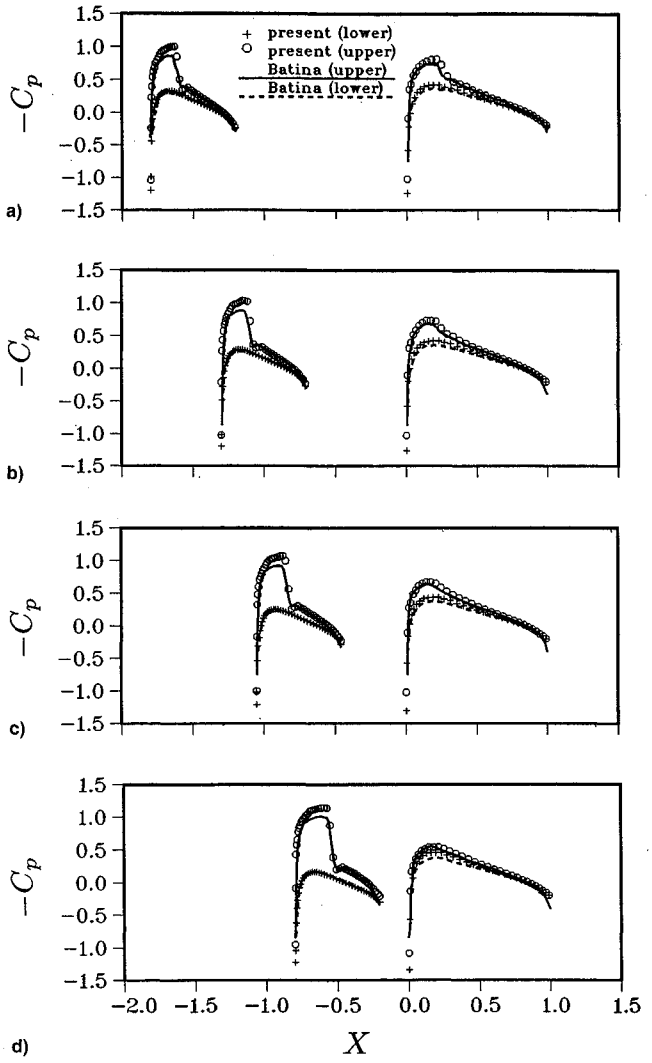

Fig. 13 Pressure distribution for different horizontal distances, S = a) 2.0, b) 1.5, c) 1.25, and d) 1.0.

IV. Canard-Wing Interference

In this section, we present the results of two-dimensional canard-wing aerodynamic interference in steady and unsteady transonic flows to demonstrate the robustness of the numerical algorithm, and qualitative and qualitative aerodynamic influence of one airfoil on the other.

A. Steady Canard-Wing Interference

The model consisted of two NACA 0010 airfoils which are arranged in tandem. A schematic of the arrangement is shown in Fig. 11. In this figure the canard chord length is selected to be 60% of the wing chord length, S (normalized by the wing chord length) is the horizontal distance between the midchords of wing and canard, and the vertical distance is fixed at 0.25. We study four different cases: S = 2.0, S =

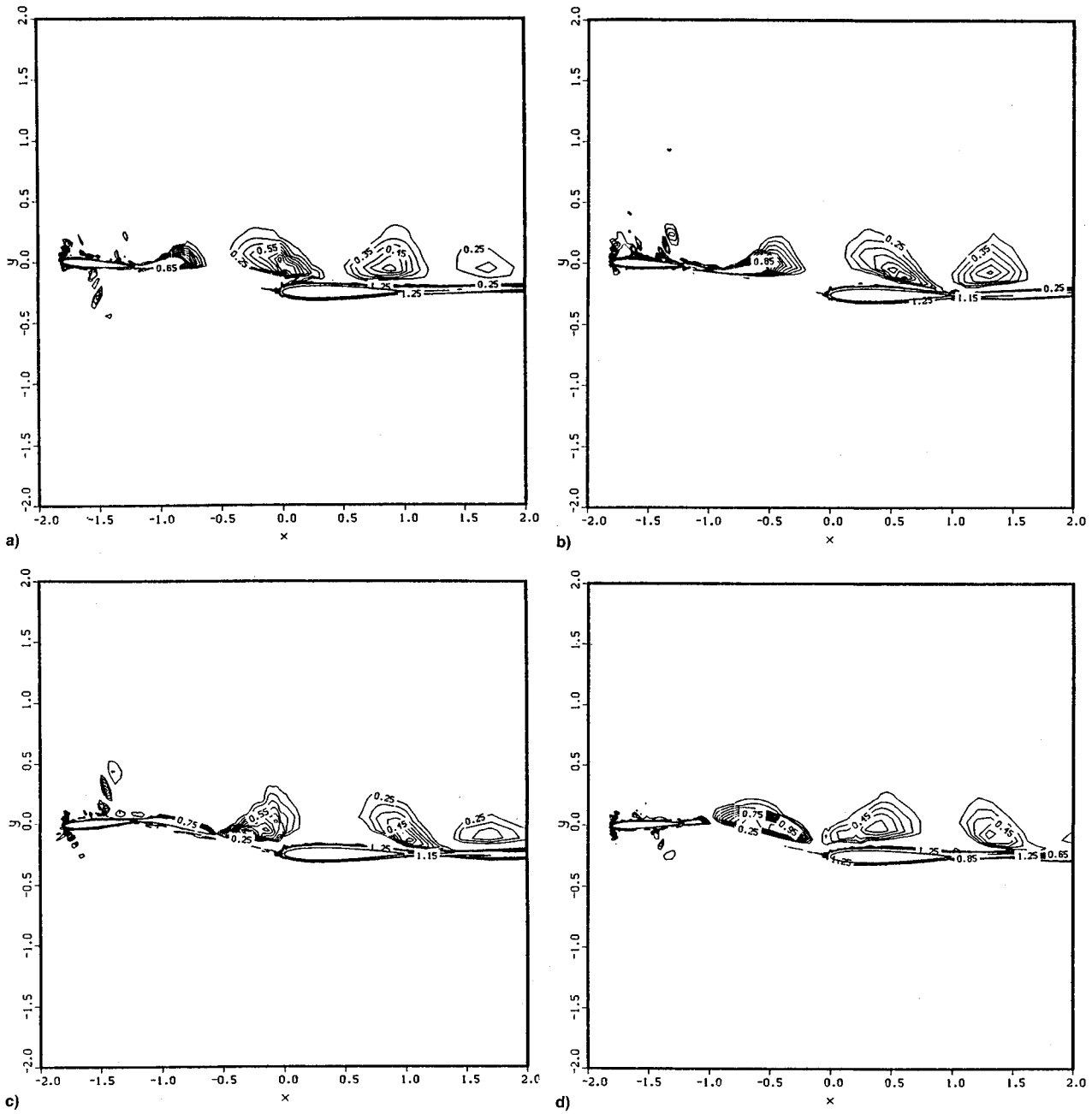

Fig. 14 Vorticity contour at phase angle: a) $50\pi/6$, b) $53\pi/6$, c) $56\pi/6$, and d) $59\pi/6$.

1.5, $S = 1.25$, and $S = 1.0$ in order to understand the effect of canard-wing interaction at different separate distance. The flow conditions considered are $\alpha = 1$ deg, $M_\infty = 0.76$. For the grid system, we distribute 81 and 65 points on the canard and wing, and use 237 × 21, 217 × 21, 217 × 21, and 207 × 21 C-type grids for the different horizontal separation $S = 2.0$, 1.5, 1.25, and 1.0, respectively. Also, Δx_{min} on the leading edge of canard is 4.24×10^{-3}, Δx_{min} on the trailing edge of canard is 1.27×10^{-2}, Δx_{min} on the leading edge of wing is 8.0×10^{-3}, and Δx_{min} on the trailing edge of wing is 2.0×10^{-2}. In the normal direction of airfoil in the canard-wing case, we gave $\Delta y_{min} = 5.0 \times 10^{-3}$. Figure 12 shows the grid system for the case, $S = 1.0$.

The computational results of pressure distribution are presented in Fig. 13. Our computational results agree with Batinar's,[4] except at the upper canard surface on which there is a stronger effect obtained by the Euler model. This meant that the isentropic TSD model may not be good enough. Whitlow[17] pointed out that one may use nonisentropic corrections to improve the potential model. By comparing the pressure distribution on an isolated airfoil and canard-wing configuration, we can find some phenomena. For this configuration the canard produces a downwash on the wing that weakens the shock strength. Conversely, the wing produces an upwash on the canard, such that the shock strength is increased on the upper surface of canard. As the horizontal separation distance between two airfoils becomes small, the shock on the upper surface of the canard is increased in strength, and the shock on the upper surface of wing is decreased in strength. To satisfy the Kutta condition, we can consider the canard as a stationary vortex in front of the wing, that produces a downwash on the wing and decreases the effective angle of attack for the wing. Therefore, the lift on the wing would be lower than a single wing. Similarly, the wing produces a circulation to induce an upwash on the canard thus increasing the lift of canard.

B. Unsteady Canard-Wing Interference

For this problem, the pitching motion of the canard is similar to the single airfoil case: $\alpha_m = 1$ deg, $\alpha_0 = 5$ deg, $k = 1$, and $M_\infty = 0.76$. Two cases of different horizontal separation distance, $S = 2.0$ and $S = 1.25$, are investigated in

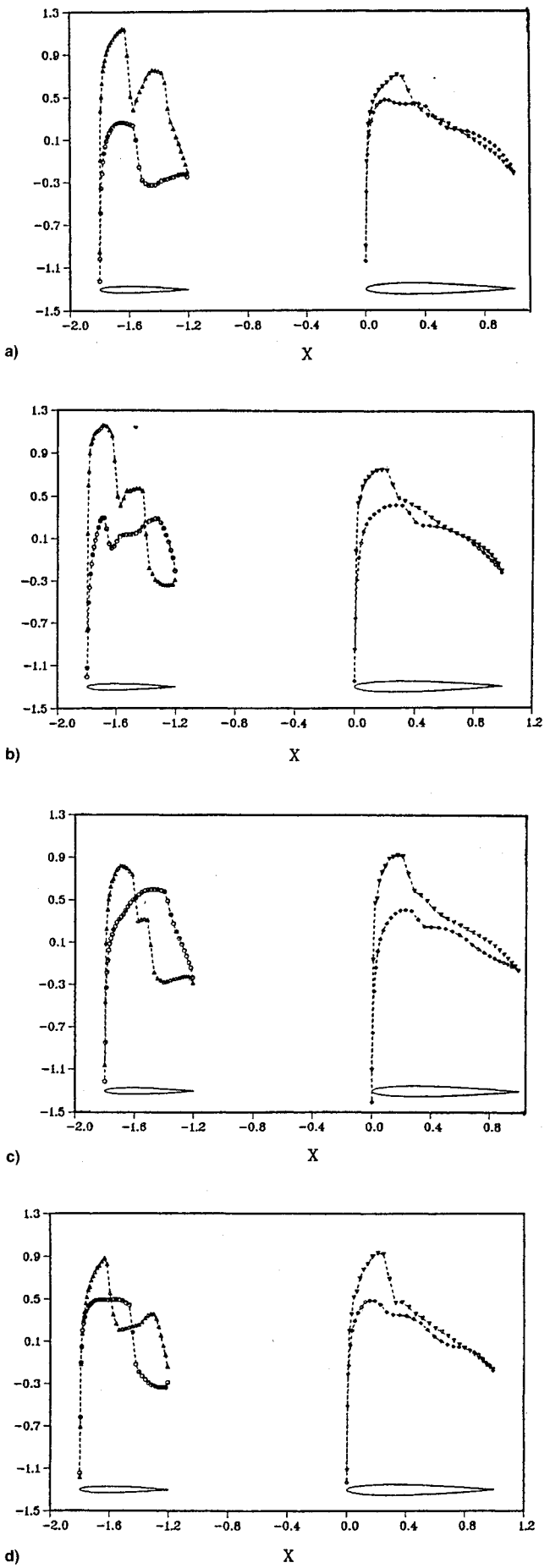

Fig. 15 Pressure distribution at phase angle: a) $50\pi/6$, b) $53\pi/6$, c) $56\pi/6$, and d) $59\pi/6$.

this study. Our computational results indicate that the pressure distribution of the 10π phase angle matches well with the 8π phase angle, so we assume that the flowfield becomes periodic after four cycles of pitching motion.

For $S = 2.0$, Fig. 14 shows the vorticity contours during the 5th cycle. One can see that the vortices shed from the tail of the canard, follow the flow stream, and go through the upper surface of the wing to the downstream. From the Kelvin's theorem we know when the canard is pitching up, the circulation around the canard will increase, and when a counterclockwise trailing vortex will be induced and shed. Inversely, when the canard is pitching down, a clockwise trailing vortex is induced and shed. In Fig. 14, at the phase angle of $56\pi/6$, there is a counterclockwise vortex ahead of the wing and a clockwise vortex behind the wing. These two vortices offer the wing extra lift. Inversely, at the phase angle $50\pi/6$, there is a clockwise vortex ahead of the wing and a counterclockwise vortex behind the wing, they induce the downward force and decrease the lift of wing. We can conclude that during the 5th cycle the maximum and minimum lift coefficients on the wing occur at phase angles of $56\pi/6$ and $50\pi/6$, respectively. Figure 15 shows the pressure distribution on the airfoil surfaces. One can see that there are local changes on the upper surface of wing around the shock region and the variation of lower surface of the wing is small.

For the canard-wing configuration with $S = 1.25$, the similar phenomena occur, except that the interference between the wing and canard is stronger and the maximum and minimum lift coefficients on the wing occur at phase angles of $52\pi/6$ and $57\pi/6$, respectively.

V. Conclusions

In this article we apply the discontinuous finite element method coupling with a dynamic grid algorithm to study the steady/unsteady, inviscid/viscous flows passing through single/canard-wing airfoils. The accuracy of the method is investigated for flows past a NACA 0012 airfoil with/without pitching motions and an airfoil-vortex interaction. A fairly good agreement by comparisons with related numerical data is obtained. The results of steady canard-wing configuration computations show that the canard induces a downwash on the wing and decreases its lift. Conversely, the wing induces an upwash on the canard that increases its lift. About the unsteady canard and wing interaction, our studies show that there is an upwash acting on the wing when the counterclockwise shedding vortex is ahead of the wing or a clockwise shedding vortex is behind it, and the wing will obtain extra lift. Inversely, with a clockwise vortex ahead of the wing or a counterclockwise vortex behind it, a downwash acts on the wing and decreases the lift. The results of two-dimensional canard-wing aerodynamic interference on steady and unsteady transonic flows demonstrate the robustness of the numerical algorithm, and qualitative and quantitative aerodynamic influence of one airfoil on the other.

Acknowledgments

The authors gratefully acknowledge the support of the National Science Council of the Republic of China and they thank the reviewers and the associate editor for their helpful comments.

References

[1]Shankar, V., Malmuth, N., and Cole, J., "Transonic Flow Calculations over Two-Dimensional Canard-Wing System," AIAA Paper 79-1565, July 1979.

[2]Shankar, V., and Malmuth, N., "Computational Treatment of Transonic Canard-Wing Interactions," AIAA Paper 82-0161, Jan. 1982.

[3]Agrell, N., and Elmeland, L., "Transonic Aerodynamic Computations for a Canard Configuration," *Journal of Aircraft*, Vol. 22, No. 8, 1985, pp. 675–678.

[4]Batina, J. T., "Unsteady Transonic Flow Calculations for Two-

Dimensional Canard-Wing Configurations," *Journal of Aircraft*, Vol. 23, No. 4, 1986, pp. 290–298.

[5]Batina, J. T., "Unsteady Transonic Flow Calculations for Interfering Lifting Surface Configurations," *Journal of Aircraft*, Vol. 23, No. 5, 1986, pp. 422–430.

[6]Lin, S. Y., and Chin, Y. S., "Discontinuous Finite Element Method for Two Dimensional Conservation Laws," *AIAA Journal*, Vol. 31, No. 11, 1993, pp. 2016–2026.

[7]Batina, J. T., "Unsteady Euler Airfoil Solution Using Unstructured Dynamic Meshes," *AIAA Journal*, Vol. 28, No. 8, 1990, pp. 1381–1388.

[8]Batina, J. T., "Implicit Flux-Split Euler Schemes for Unsteady Aerodynamic Analysis Involving Unstructured Dynamic Meshes," *AIAA Journal*, Vol. 29, No. 9, 1991, pp. 1836–1843.

[9]Lu, P. J., and Yeh, D. Y., "Transonic Flutter Suppression Using Active Acoustic Excitations," AIAA Paper 93-3285, July 1993.

[10]Swanson, R. C., and Turkel, E., "A Multistage Time-Stepping Scheme for the Navier-Stokes Equations," AIAA Paper 85-0035, June 1985.

[11]Harris, C. D., "Two-Dimensional Aerodynamic Characteristics of the NACA0012 Airfoil in the Langley 8-Foot Transonic Transonic Pressure Tunnel," NASA TM 81927, April 1981.

[12]Thibert, J. J., Granjacques, M., and L. H. Ohman, "NACA 0012 Airfoil, AGARD Advisory Report No. 138, Experimental Data Base for Computer Program Assessment," 1979, pp. A1–9.

[13]Landon, R. H., "NACA 0012 Oscillatory and Transient Pitching," Compendium of Unsteady Aerodynamic Measurements, Data Set 3, AGARD-R-702, Aug. 1982.

[14]Kandil, O. A., and Chuang, H. A., "Unsteady Transonic Airfoil Computation Using Implicit Euler Scheme on Body-Fixed Grid," *AIAA Journal*, Vol. 27, No. 8, 1989, pp. 1031–1037.

[15]Caradonna, F. X., Desopper, A., and Tung, O., "Finite-Difference Modeling of Rotor Flows Including Wake Effects," NASA TM-84280, 1982.

[16]McCroskey, W. J., and Goorjian, P. M., "Interactions of Airfoils with Gusts and Concentrated Vortices in Unsteady Transonic Flow," AIAA Paper 83-1691, July 1983.

[17]Whitlow, W., Jr., "Application of a Nonisentropic Full Potential Method to AGARD Standard Airfoils," AIAA Paper 88-0710, Jan. 1988.